Acta Biomaterialia 8 (2012) 3360–3371

Contents lists available at SciVerse ScienceDirect

Acta Biomaterialia

journal homepage: www.elsevier.com/locate/actabiomat

Continuum modeling of a neuronal cell under blast loading

Antoine Jérusalem [a,*], Ming Dao [b,*]

[a] IMDEA Materials Institute, C/ Profesor Aranguren s/n, 28040 Madrid, Spain
[b] Massachusetts Institute of Technology, 77 Massachusetts Avenue, Cambridge, MA 02139, USA

ARTICLE INFO

Article history:
Received 27 January 2012
Received in revised form 2 April 2012
Accepted 25 April 2012
Available online 2 May 2012

Keywords:
Continuum model
Neuron
Blast
Cell damage
Traumatic brain injury

ABSTRACT

Traumatic brain injuries have recently been put under the spotlight as one of the most important causes of accidental brain dysfunctions. Significant experimental and modeling efforts are thus underway to study the associated biological, mechanical and physical mechanisms. In the field of cell mechanics, progress is also being made at the experimental and modeling levels to better characterize many of the cell functions, including differentiation, growth, migration and death. The work presented here aims to bridge both efforts by proposing a continuum model of a neuronal cell submitted to blast loading. In this approach, the cytoplasm, nucleus and membrane (plus cortex) are differentiated in a representative cell geometry, and different suitable material constitutive models are chosen for each one. The material parameters are calibrated against published experimental work on cell nanoindentation at multiple rates. The final cell model is ultimately subjected to blast loading within a complete computational framework of fluid–structure interaction. The results are compared to the nanoindentation simulation, and the specific effects of the blast wave on the pressure and shear levels at the interfaces are identified. As a conclusion, the presented model successfully captures some of the intrinsic intracellular phenomena occurring during the cellular deformation under blast loading that potentially lead to cell damage. It suggests, more particularly, that the localization of damage at the nucleus membrane is similar to what has already been observed at the overall cell membrane. This degree of damage is additionally predicted to be worsened by a longer blast positive phase duration. In conclusion, the proposed model ultimately provides a new three-dimensional computational tool to evaluate intracellular damage during blast loading.

1. Introduction

The drastic increase in blast-induced traumatic brain injuries among both military (nearly 50% of the Iraq war injured returnees) and civilian casualties – mainly due to terrorists explosive devices – have generated important research efforts in the last few years [1,2]. Impact- and/or acceleration-induced brain traumatic injuries have already been the focus of many cellular and macroscopical studies through in vivo [3–10], ex vivo [11,12], in vitro [13–17], medical postanalysis [18–21] and modeling approaches [22–35]. However, the specific effects of a blast – a pressure wave of finite amplitude generated by a rapid release of energy [36] – on the brain is still widely unknown.

Blast overpressure, or "primary", injuries have been known for close to 70 years, and have since been extensively observed in the lungs, eyes, ears, upper respiratory tract, heart, abdomen and more recently brain [37]. The recent wars in Iraq and Afghanistan have further exacerbated the awareness of the existence of specific mechanisms of blast injuries in the brain [38,1,39]. Many neuropathological and neurological injuries have already been referenced for both animal models and humans [2]. At the cellular level, degradation of the cytoskeleton, changes in neurotransmitters, disruption of calcium homeostasis, mitochondrial disturbances, loss in membrane permeability and even altered gene expression have been observed [39,17]. More specifically, studies of cellular response after blast events provide evidence of degenerative processes in the neuron itself, not only through necrotic pathways but also through apoptotic pathways – or programmed cell death, at the origin of most brain dysfunctions [40,39,2].

Technical improvements now allow for the in vivo study of direct blast effects on animal brain without significantly invading the brain tissue [41,42], as well as ex vivo study to quantify the accompanying functional damage [12]. Additionally, a vast array of in vitro techniques, involving barotrauma chamber, rapid acceleration injury device or shock wave generator, allow for more flexibility, though at the cost of not taking into account the real environment provided under in vivo settings [43,44]. A wider set of experiments, ranging from simple stretch and isostatic pressurization to weight drop and stylus laceration, are also available to account for non-primary blast injuries, i.e. blast injuries arising

* Corresponding authors.
E-mail addresses: antoine.jerusalem@imdea.org (A. Jérusalem), mingdao@mit.edu (M. Dao).

1742-7061/$ - see front matter © 2012 Acta Materialia Inc. Published by Elsevier Ltd. All rights reserved.
http://dx.doi.org/10.1016/j.actbio.2012.04.039

from direct impact or penetration (secondary), collision arising from a fall of or onto the subject (tertiary), or exposure to gas, fire or similar (quartenary) [44]. Moreover, a recent study has directly compared in vivo, in situ and in vitro brain responses to different indentation rates [45], thus paving the way for more realistic constitutive models of brain tissue under high rate loadings. Coupled to these improvements in experimental testing, new imaging techniques can now achieve submicrometer resolution [46].

In parallel to these experimental efforts, recent complex large-scale parallel computational models accounting for fluid–solid interaction effects between the air blast and multiple organs in the cranium now allow for pressure extrema localization, and identification of more complex electromagnetic coupling effects with a very high precision [47–50].

At the cellular level, many groups have focused their efforts on the development of mechanical models of the deformation of individual cells or cell parts [34,51–81]. For instance, significant progress has been made on red blood cell (RBC) modeling, with full three-dimensional (3-D) models using finite-element-based continuum methods [55,66], coarse-grained molecular dynamics (MD) simulations [82,83], and dissipative particle dynamics (DPD) computations capable of describing detailed cell–fluid interactions [84]. These RBC models have been successfully applied to study diseases such as malaria [84,85]. Developing computational models for cells with a nucleus and a 3-D cytoskeleton network, however, has been much more challenging than for RBCs, which have a much simpler cytoskeletal structure and no nucleus.

Among the different techniques proposed in the literature to describe the mechanics of living cells with a nucleus and a 3-D cytoskeleton, the most notable involve: modeling the cytoskeleton as a simple mechanical elastic, viscoelastic or poroviscoelastic continuum [61,62], as a porous gel or soft glassy material [70], or as a "tensegrity" network incorporating discrete structural elements that bear compression [71]. At a smaller scale, cytoskeleton proteins and their interaction with the membrane have been more recently modeled using MD, coarse-grained MD and normal mode analysis [86–88]; however, the important length and time scale limitations of MD, coupled with the large number of unknowns either for the atomic interaction potentials or the protein interaction mechanisms, prevent its use at the cellular scale. Overall, it is observed that continuum models are flexible enough to allow for a relatively accurate representation of the geometry of cell parts (e.g. nucleus, cytoplasm and membrane/cortex), together with the individual macroscopic features of the deformation [51,52,54,57,63–65,67,68,70–74,35,80,76,81,77].

With a few notable exceptions, very little work has been dedicated to using such models under damaging – or, at least, high – rate loading conditions [34,77,78,80]. Such studies more often than not bring additional unknowns to the problem, but under loading rates fast enough to generally avoid the active deformation of the cell, i.e. the self-reorganization of its protein structures under external stimuli. As a consequence, continuum models a priori provide an adequate framework for neuron modeling under blast loading. Finally, to the best of our knowledge, direct simulations of the damaging effects of a blast on a cell with differentiated components has still not been achieved (note that Miller et al. presented a model of a cell subjected to stress waves but focused on cell–substrate decohesion [89,77]).

In this work, we thus propose a continuum model with differentiated nucleus, cytoplasm and membrane/cortex. Each one of these components is described by a visco-hyperelastic constitutive model. These models are purposefully chosen to be as simple as possible to adequately describe the different deformation mechanisms while reducing the size of the model parameters space. Each model is calibrated against published nanoindentation experimental results at multiple rates [78] and a fluid–structure interaction continuum model of the calibrated cell is submitted to a blast wave. Section 2 introduces the constitutive framework and the finite element set-up for the simulations. The calibration of the model against experimental nanoindentation work is presented in Section 3 and the final blast simulation is shown in Section 4. Finally, the results are discussed and related to experimental studies in Section 5.

2. Numerical set-up

In this section, the visco-hyperelastic constitutive framework of all three modeled components is presented, followed by a description of the finite element model discretization and parametrization.

2.1. Constitutive framework

2.1.1. General equations

The three main modeled cell components (membrane/cortex, cytoplasm and nucleus) are assumed to follow a visco-hyperelastic mechanical behavior.

For isotropic hyperelastic materials, it is generally assumed that a Helmholtz free energy function Ψ can be defined as a function of the Jacobian J and the modified strain invariants $\bar{I}_1$ and $\bar{I}_2$ [90].

The stress measure conjugated to the right Cauchy–Green tensor $\mathbf{C}$, the second Piola Kirchhoff stress $\mathbf{S}$, is then given by

$$\mathbf{S} = 2\frac{\partial \Psi}{\partial \mathbf{C}} \tag{1}$$

2.1.2. Generalized Maxwell model

The viscoelastic formulation used here is based on the work of Taylor et al. [91].

The generalized Maxwell model is a rheological model composed of a Hooke model (i.e. a spring) and a given number of Maxwell models – a Hooke model and a Newton model (i.e. a dashpot) in series – in parallel [92]. In order to minimize the number of model parameters, we couple the hyperelastic model defined earlier with a generalized Maxwell model composed of only one Maxwell component (see Fig. 1). It is the simplest model that allows consideration of both long-term and short-term elasticity with a viscous effect.

In Fig. 1, μ_0, μ_1 and η_1 are respectively the long-term shear modulus, and the shear modulus and viscosity associated with the Maxwell component. $\mathbf{\Gamma}$ is the internal variable, a strain measure, associated with the dashpot, and $\mathbf{S}_{iso} = \mathbf{S}_{vis} + \mathbf{S}^{\infty}_{iso}$ is the isochoric second Piola Kirchhoff stress defined as the sum of its viscous and long term components. This first tensor characterizes the viscous relaxation due to a viscous Newtonian fluid, and is representative here of all viscous effects arising in each one of the three components of the cell. It should be noted that these effects are restricted to the isochoric deformation mode. For more details on theory and implementation, see Ref. [90].

2.1.3. Neo-Hookean model

As already stated, the work presented here is aimed at minimizing the number of parameters. As a consequence, the neo-Hookean

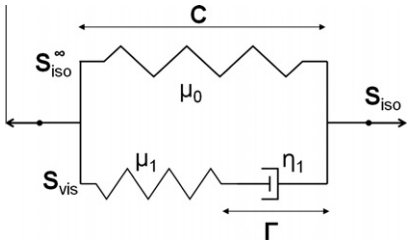

Fig. 1. First-order generalized Maxwell model.

model is chosen for all cell components. This model depends only on the Jacobian and the first strain invariant. The associated long-term volumetric and isochoric strain energy functions are given by [90]

$$\begin{cases} \Psi^{\infty}_{vol}(J) = \frac{1}{d_0}(J-1)^2 \\ \Psi^{\infty}_{iso}(\bar{I}_1) = c_0(\bar{I}_1 - 3) \end{cases} \tag{2}$$

where $c_0 = \mu_0/2$ (see Section 2.1.2), and d_0 is a material parameter related to the compressibility of the material.

2.1.4. Hugoniot/Mie-Grüneisen equation of state

As long as relatively low strain rates and pressures are considered, the above description is reliable. However, when very fast material responses under high pressures are considered, such as the ones provoked by a shock wave, the volumetric part of the stress tensor, i.e. the pressure P, must be described by an equation of state. As a consequence, even though such an approach is not necessary for the indentation simulation, it is required for the blast simulation.

The shock response of many materials is described well by the Hugoniot relation between the shock velocity U_s and the material velocity U_p of the simple form [93]:

$$U_s = C_0 + sU_p \tag{3}$$

In this expression, C_0 and s are material parameters which can be obtained from experiments.

By considering conservation of mass and momentum in a control volume at the shock front and Eq. (3), the final pressure[1] can be calculated explicitly as a function of the Jacobian behind the shock front J_H and the reference density ahead of the shock ρ_0 [94]:

$$P_H = \frac{\rho_0 C_0^2 (1 - J_H)}{[1 - s(1 - J_H)]^2} \tag{4}$$

where J_H is related to the density ρ_H, the specific volume V_H or the deformation gradients tensor $\mathbf{F}_H$, defined behind the shock front, by:

$$J_H = \frac{\rho_0}{\rho_H} = \frac{V_H}{V_0} = det(\mathbf{F}_H) \tag{5}$$

Alternatively, one can use the Mie-Grüneisen equation of state to relate the pressure P and the internal energy per unit mass E to their respective value on the Hugoniot curve P_H and E_H [93], which leads to

$$P = P_H\left(1 - \frac{\Gamma_0}{2}\left(1 - \frac{\rho_0}{\rho}\right)\right) + \Gamma_0 \rho_0 E \tag{6}$$

where Γ_0 is the Grüneisen parameter in the initial state.

Finally, the internal energy rate per unit mass is given by the first law of thermodynamics as the sum of the volumetric and deviatoric work rates, and heat rate $\dot{Q}$ [93]:

$$\dot{E} = -\frac{1}{\rho}\left(\frac{P\dot{\rho}}{\rho} + \dot{\Psi}_{iso}\right) + \dot{Q} \tag{7}$$

where use has been made of the deviatoric strain energy function, and where C_v is the specific heat capacity at constant volume and T is the temperature.

Additionally, the shock response can be considered as an adiabatic process: $\dot{Q} = 0\ \mathrm{J\,kg^{-1}\,s^{-1}}$. Note that the pressure release is actually isentropic, in general relatively close to the adiabatic process; as a consequence, the whole event can indeed be assumed as adiabatic [93].

The temperature can then be extracted easily from:

$$\dot{E} = C_v \dot{T} \tag{8}$$

An artificial viscosity scheme (necessary for shock wave propagation) is finally used (a complete description is provided in Supplementary materials A-3).

2.2. Finite element model

The main components that regulate the mechanical properties of the cell are the membrane, the cytoplasm (composed of the cytoskeleton and organelles bathed in a rheological fluid: the cytosol) and the nucleus [62]. The cytoskeleton is a dynamic structure that maintains the cell shape, protects it, enables cellular motion and plays an important role in all cellular processes. It contains three main mechanical structures with different functionalities: actin filaments, intermediate filaments and microtubules. The cell membrane is a semipermeable lipid bilayer that separates the interior of the cell from the outside. The cytoskeleton is found underlying the cell membrane in the cytoplasm and provides a scaffold for membrane proteins to anchor to, as well as enabling the formation of organelles that extend in and out of the cell. In fact, cytoskeletal elements interact extensively and intimately with the cell membrane, creating a region, just beneath the membrane, that is densely populated with proteins: the cortex [95]. Finally, the cell nucleus contains most of the cell's genetic material and is therefore the control center of the cell.

In the following, we detail the finite element discretization set-up for the calibration (nanoindentation) simulations and for the blast simulation. The commercial finite element software Abaqus was used for the simulations [96].

2.2.1. Nanoindentation finite element set-up

We propose here to follow the same overall geometry of a semi-spheroid as in Ref. [78], but focusing more on the intrinsic structures of the neuron, while simplifying the constitutive models for each modeled part, rather than adopting a more complex representative constitutive law for the whole neuron cell. The chosen modeled continua are the nucleus, the cytoplasm and the cortex plus membrane, see Supplementary materials A.

The model size is based on the average height and diameter observed experimentally (from 79 observations) by Bernick et al. [78]: a height of 7.9 μm for a diameter of 16.8 μm. The nucleus is then considered as having a volume of one-third of the total cell volume [67]. Its dimensions are chosen such that the ratio of the diameters and heights of the full neuron cell and the nucleus are the same, i.e. the diameter and height are respectively 11.65 and 5.48 μm. The nucleus is centered in the middle of the cell. The thickness of the "membrane plus cortex" region is estimated to be in the range of 100–400 nm [59,62]. For simplicity, a compromise value of 200 nm is chosen here. For the indentation simulation, the axisymmetry of the problem allows for the use of a 2-D axisymmetric mesh. The final mesh is shown in Fig. 2. More details on the regions of interest, geometry and finite element mesh are given in Supplementary materials A-1.

The boundary and loading conditions follow the set-up used in Ref. [78]. The bottom part is fixed in all directions, consistent with the experimental observation that the neuron is in slipless contact with its substrate [78]. The usual axisymmetric boundary conditions are specified along the axis of revolution. Finally, a 45 μm diameter spherical bead is used for the nanoindentation and is modeled as an analytical rigid surface. The loading pattern is as follows: a first indentation at 0.3 $\mu m\,s^{-1}$ until a force of roughly 0.3 nN is measured; a plateau at the same position for 15 s; three load–unload cycles to 2 μm additional depth at three increasing rates, 10, 1 and 0.1 $\mu m\,s^{-1}$; a final load at 10 $\mu m\,s^{-1}$ and a plateau

[1] In this section only, the pressure is by convention positive in compression.

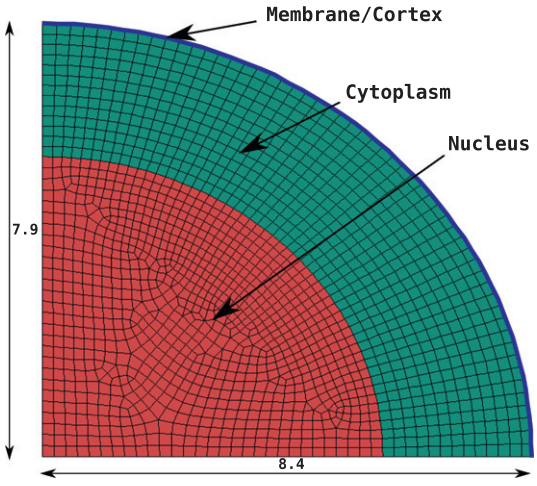

Fig. 2. 2-D axisymmetric mesh of the neuron used for nanoindentation (distances in μm).

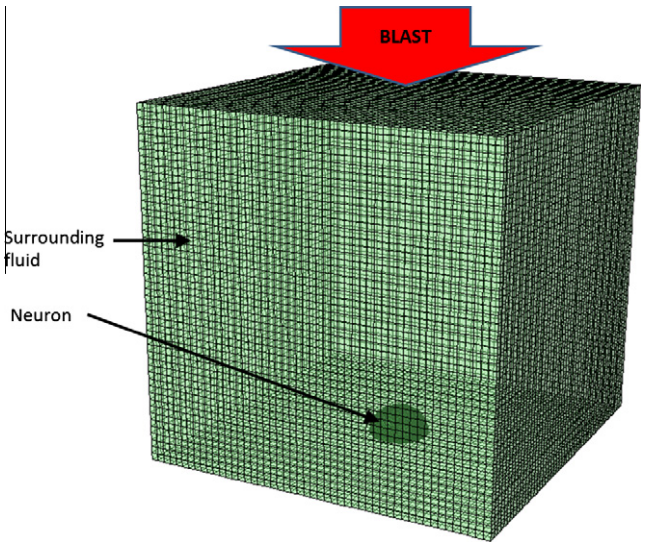

Fig. 3. Finite element set-up of the blast simulation.

at this depth for 120 s. See Ref. [78] for more details. Table 1 presents the different loading steps used in this reference.

A static implicit scheme is used for the nanoindentation simulation. Spatial convergence was verified. Note that the rates are small enough to ignore any inertial effect (the Reynolds numbers for the different model parts are in the range of 2×10^{-17}–10^{-7}), thus there is no need for dynamic simulations in this case.

2.2.2. Blast finite element model set-up

For the blast simulation, the previous cell model geometry is extended to three dimensions, with the same height and diameter and embedded at the bottom of a 100 μm × 100 μm × 100 μm cubic fluid box. The final model is shown in Fig. 3. More details are given in Supplementary materials A-2.

The overpressure loading of a shock wave as emitted by a shock tube is typically of the order of hundreds of kPa (i.e. a few atm) with duration of the order of 1 ms [97]. However, recent in vitro studies have used laser-induced shock waves to study cell injury [98], as well as cell adhesion [89,77]. For such waves, the overpressure is of the order of 50 MPa [98] and the duration of the order of 5 ns for a Gaussian laser pulse [89].

Because the work proposed here is oriented towards the comparison of simulations with in vitro experiments, the pressure pulse used on the top face of the model follows the latter description: a constant applied pressure of 50 MPa for 5 ns.

3. Nanoindentation simulation

An extensive survey of the model parameter values that can be found in the literature is provided in Supplementary materials B.

The three cell components are considered to be incompressible, as is commonly assumed for biological cells [52,53,56,55,61,63,73,75–79]. Based on this incompressibility, the Poisson's ratio is taken to be $\nu = 0.5$ ($d_o = 0$) for all regions. It should be emphasized, though, that other studies have suggested compressibility [99,74,81], in some cases with significant effects on the deformation mechanisms [74]. However, in view of the lack of consensus and the fact that, under shock loading (see Section 4), there is a priori not enough time for viscosity and/or volume change to occur, this value of 0.5 is chosen as a first approximation.

In view of the literature review, the value of 1000 Pa is chosen for the membrane/cortex Young's modulus ($c_0^{mem} = 166.67\ Pa$) and the relaxation time τ_1^{mem} is taken as 3000 s (see Supplementary materials B-1). In the following, we determine the remaining parameters by calibrating them against the averaged experimental nanoindentation curve of Ref. [78], and validate them by comparing simulation and experiment for another cell-specific nanoindentation test [78].

It should finally be emphasized that in the proposed model the adhesion between cell and bead is not taking into account as a first approximation; for a modeling approach accounting for it, see Ref. [72].

3.1. Initial indentation depth and calibration of the Young's moduli

As described in Section 2.2.1, the initial loading rate (0.3 μm s^{-1}) is maintained until $F_B = 0.3$ nN is reached (stages A and B in Table 1). Depending on the cell height, the indentation depth at which this load is reached consequently varies. Additionally, the final plateau of the loading at stage E yields an approximate force of $F_E = 1.67$ nN in the average experimental curve [78].

Note that Hertz's contact law does not apply here because of the multiple material stiffnesses of the cell regions. Both plateaux of stages B and E reach a steady-state value that is independent of viscosity by definition. As such, the only two remaining parameters of influence are the Young's moduli of the cytoplasm and the nuclei, E_0^{cyto} and E_0^{nuc}. Assuming a factor of 4 difference between the two values (see Supplementary materials B-2), the set of unknown values defining both plateaux is narrowed down to two parameters only: δ_0 and E_0^{nuc} (or E_0^{cyto}). Additionally, assuming that the contact

Table 1
Nanoindentation loading cycles followed by Bernick et al. [78] (rates are given in μm s^{-1}; "0", "+" and "–" refer to a plateau, loading and unloading, respectively, between the initial indentation depth δ_0 at Steps A and B to $\delta_0 + 2$ μm).

Cycles	A	B	C_1						C_2						C_3						D	E
Load	+	0	+	–	+	–	+	–	+	–	+	–	+	–	+	–	+	–	+	–	+	0
Rate	0.3	0	10						1						0.1						10	0

is made in a similar way to Hertz's law but leaving the exponent n (fixed at 3/2 in Hertz's law) as a free parameter, one reaches:

$$\frac{\delta_0 + 2}{\delta_0} = \left(\frac{F_E}{F_B}\right)^n \tag{9}$$

This relation mathematically guarantees that the pair of unknowns (δ_0, E_0^{nuc}) is uniquely defined by the pair (F_B, F_E). After calibration, we finally reach:

$$\begin{cases} \delta_0 = 1.41\ \mu m \\ c_0^{nuc} = E_0^{nuc}/6 = 6.67\ Pa \\ c_0^{cyto} = E_0^{cyto}/6 = 1.66\ Pa \end{cases} \tag{10}$$

Note that the nucleus and cytoplasm values are in the lower range of the literature values (see Supplementary materials B-2).

3.2. Calibration of the viscosity parameters

Because all the cell parts are taken as incompressible, the viscosity parameters are defined only for the shear component. The main difficulty of this calibration resides in the fact that five parameters need to be defined: the relaxation times τ_1^{nuc} and τ_1^{cyto}, the viscosities η_1^{nuc} and η_1^{cyto} for nucleus and cytoplasm, and also η_1^{mem} for the membrane/cortex. By considering that the factor of 4 between the long-term shear moduli of cytoplasm and nucleus is also valid for the shear moduli associated with the Maxwell components μ_1 (see Fig. 1), the space of the parameters is reduced to four unknowns: τ_1^{nuc}, τ_1^{cyto}, η_1^{nuc} (or η_1^{cyto}) and η_1^{mem}. Note that picking a pair (τ_1, η_1) is equivalent to picking (τ_1, μ_1); in the following we use the latter.

Despite the fact that simple viscous models have been chosen, the number of unknowns is relatively high. However, the advantage of having three cycles and two relaxation periods to fit the model is that each parameter is observed to influence the simulated curve in different ways. Without being able to fully guarantee the uniqueness of the parameters, we empirically observed that, around the final chosen values, changes in τ_1^{nuc} and τ_1^{cyto} affect the relaxation of the fast and slow cycles, respectively, while μ_1^{nuc} (or μ_1^{cyto}) affects the peak values of the reaction forces at the maximum indentations, and μ_1^{mem} affects most of the curve, albeit more lightly. As a consequence, most of the parameters have been calibrated by considering their action on the reaction–indentation curve patterns independently, μ_1^{mem} being used to finalize the final fit. The final set of parameters is given in Table 2, and the set of curves for the three simulated cycles (done successively within the same simulation, as done experimentally) and the experimental curves taken from Ref. [78] are shown in Figs. 4–6. A good fit is obtained and the simulation results are well within the experimental error bars (not shown here; see Ref. [78]).

Note that the viscoelastic time constants for the nucleus and the cytoplasm $\tau_1^{nuc/cyto}$ are in good agreement with the literature values (see Supplementary materials B-2). The membrane viscosity ($\eta_1^{mem} = 41.67$ kPa s) is slightly less than an order of magnitude smaller than the literature values (375 kPa s in Supplementary materials B-1), whereas the nuclear viscosity ($\eta_1^{nuc} = 431.11$ Pa s) lies within the literature range (52–1200 Pa s in Supplementary materials B-2).

Table 2
Model parameters.

δ_0		c_0^{mem}	d_0^{mem}	μ_1^{mem}	τ_1^{mem}	c_0^{cyto}
1.41 μm		166.67 Pa	0 Pa^{-1}	13.89 Pa	3000 s	1.67 Pa
d_0^{cyto}	μ_1^{cyto}	τ_1^{cyto}	c_0^{nuc}	d_0^{nuc}	μ_1^{nuc}	τ_1^{nuc}
0 Pa^{-1}	107.78 Pa	0.01 s	13.33 Pa	0 Pa^{-1}	862.22 Pa	0.5 s

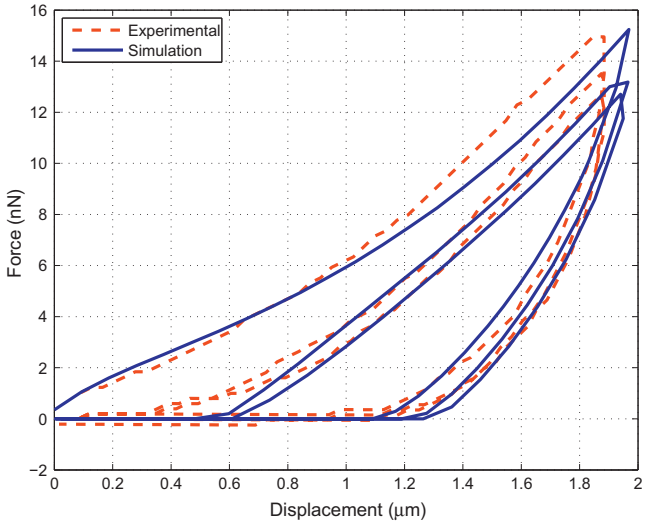

Fig. 4. Indentation force vs. displacement for the fast cycle (10 μm s^{-1}).

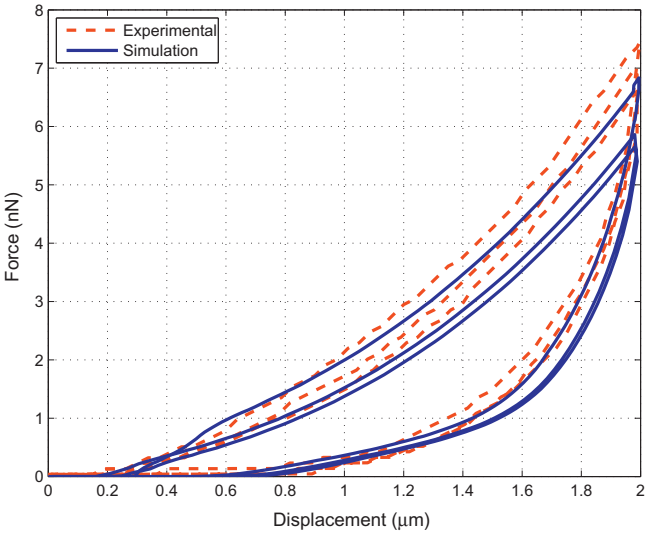

Fig. 5. Indentation force vs. displacement for the medium cycle (1 μm s^{-1}).

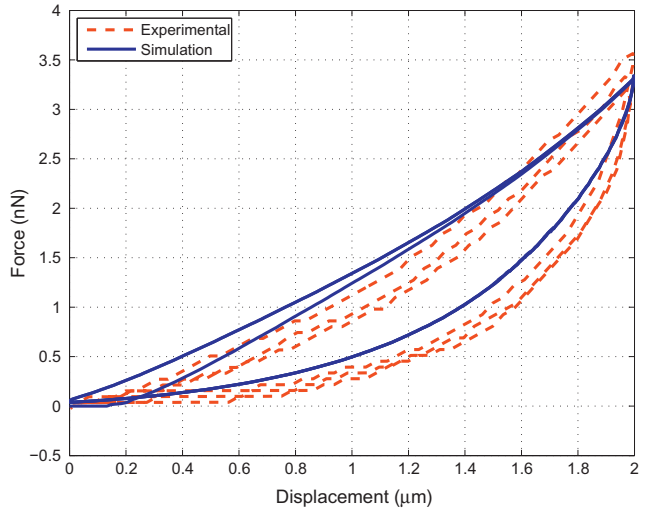

Fig. 6. Indentation force vs. displacement for the slow cycle (0.1 μm s^{-1}).

However, the cytoplasmic viscosity ($\eta_1^{cyto} = 1.08$ Pa s) is one to two orders of magnitude smaller than the full cytoplasm values (26–600 Pa s in Supplementary materials B-2), but just falls within the lower range of the crosslinked/bundled actin network (~1–500 Pa s in Supplementary materials B-2).

Finally, it should be emphasized that the literature values gathered here are from a wide range of cell types, and there is sometimes a wide range of values for the same type of cell. The observed discrepancy could be due to different experimental procedures, approximated modeling choices and/or differences in the culture of the cells. As a consequence, we complement this calibration with an additional validation step and compare simulation and experiment for an additional cell-specific nanoindentation test [78].

3.3. Validation

The validation is done by comparing the experimental results for another specific representative cell (as opposed to the average response in the previous section) with a diameter of 14.2 μm and height of 7.6 μm, similarly to what is done in Ref. [78], from which the experimental results are extracted.

The mesh presented in Section 2.2.1 was modified to account for the change in height and diameter, and all the parameters, except δ_0, were taken from Table 2. δ_0 was then adjusted to reach the inital force of 0.3 nN, and the same loading pattern as before was used for the simulation. A value 0.84 nm for δ_0 was found. The final indentation force at each of the three maxima in each of the three cycles was extracted and compared to the experimental results (see Table 3).

Taking into account the large variability in the cell geometry (including experimental error, non-constant diameter and nucleus position within the cytoplasm), the model always captures the maximum forces within 17% of the experimental value, with an overall average error of 8.4%. These results confirm the ability of the model to capture the main rate-dependent deformation features operative here.

4. Blast simulation

In the following, we use the previously calibrated model and modify the volumetric contribution of the constitutive material model following Section 2.1.4. The new material parameters are then given and the simulation is analyzed. The corresponding stress patterns are finally compared with those for the indentation.

4.1. Modifications and new material parameters

4.1.1. Surrounding fluid

As a constitutive description of the fluid deformation in the Eulerian mesh is beyond the scope of this work, we simply describe the parameters of the surrounding fluid. For more information on its implementation, see the documentation of Abaqus [96].

The Hugoniot/Mie-Grüneisen equation of state presented in Section 2.1.4 has been used successfully to describe shock wave propagation in water below 1 GPa, which is the case here [100]. Because water is the main constituent of the surrounding fluid in in vitro laser-shock experiments [98], we chose water for the surrounding fluid in the cubic box [100].

$$\begin{cases} \rho_0 = 1000 \text{ kg m}^{-3} \\ C_0 = 1450 \text{ m s}^{-1} \\ s = 1.99 \end{cases} \tag{11}$$

Additionally, for water at ambient conditions, the Grüneisen parameter, the specific heat capacity at constant volume and the dynamic (Newtonian) viscosity η are taken as [101–103]:

$$\begin{cases} \Gamma_0 \approx 0.1 \\ C_v = 4184 \text{ J kg}^{-1} \text{ K}^{-1} \\ \eta \approx 0.001 \text{ Pa s} \end{cases} \tag{12}$$

4.1.2. Neuron

As described previously, under shock loading conditions, the volumetric contribution of the stress needs to be described by an equation of state. The Hugoniot/Mie-Grüneisen has been shown to be a good candidate for the description of biomaterials submitted to shock loading [104]. Assuming the compressibility of the cell is similar to that of water (see Section 3), we use the water values for ρ_0, C_0, s, Γ_0 and C_v for the cytoplasm and nucleus. Note that, because of its shell formulation, the cortex/membrane volumetric constitutive model could not be easily replaced by an equation of state, and was kept as hyperelastic as a first approximation.

It must finally be emphasized that the deviatoric contribution of the stress is not assumed to follow the dynamic Newtonian viscosity of water, but remains the same as in the indentation model.

4.2. Simulation results

The blast simulation was run for 150 ns and the convergence was checked.

Figs. 7 and 8 show the pressure and von Mises stress fields for the different regions at 26.88 s for the nanoindentation simulation (which corresponds to the first indentation peak, with maximum pressure and von Mises stress) and 65.5 ns for the blast simulation (which corresponds to the time at which the wave has crossed half the cell, as a good compromise between the moment the wave hits the membrane and the moment it bounces back from the substrate, thus roughly doubling the pressure level). Note that maximum compression is reached at 70 ns in the blast simulation, i.e. the results shown are at almost maximum deformation. Fig. 9 shows the temperature increase for the whole cell during the blast event. Videos of the pressure field evolution during the blast for the whole mesh, as well as for the individual cell parts, are available as Supplementary materials.

Fig. 7 shows that, whereas the pressure is mainly concentrated in the cytoplasm and the top of nucleus directly underneath the indentor in the nanoindentation case, it follows the wave along the horizontal propagating plane in the blast case. Furthermore, the pressure is discontinuous in the former case at the cortex–cytoplasm (with a jump of ~300 Pa) and cytoplasm–nucleus (with a jump of ~30 Pa) interfaces, and continuous in the latter. It can thus be concluded that the blast event propagates hydrostatic stress in a less material-specific way than is done at lower rate deformations.

Interestingly, the von Mises stress levels are of the same orders of magnitude for both simulations (see Fig. 8), with maxima of ~10–100 Pa. Note that this result is even more surprising, considering that the typical cell viscosity characteristic time is of the same order of magnitude as our nanoindentation duration (seconds) [68], but much larger than that of the blast event

Table 3
Comparison between the maximum forces of an indentation experiment [78] (Exp) and simulation (Sim) for a specific representative cell; $C_{\alpha,\beta}$ refers to cycle α, maximum loading β (see Table 2).

Cycle	$C_{1,i}$	$C_{1,ii}$	$C_{1,iii}$	$C_{2,i}$	$C_{2,ii}$	$C_{2,iii}$	$C_{3,i}$	$C_{3,ii}$	$C_{3,iii}$
Exp (nN)	11.5	10.8	10.3	5	4.9	4.8	3	3	3
Sim (nN)	11.5	11	10.2	5.3	4.6	4.3	2.5	2.5	2.5
Error (%)	0	2	1	6	6	10	17	17	17

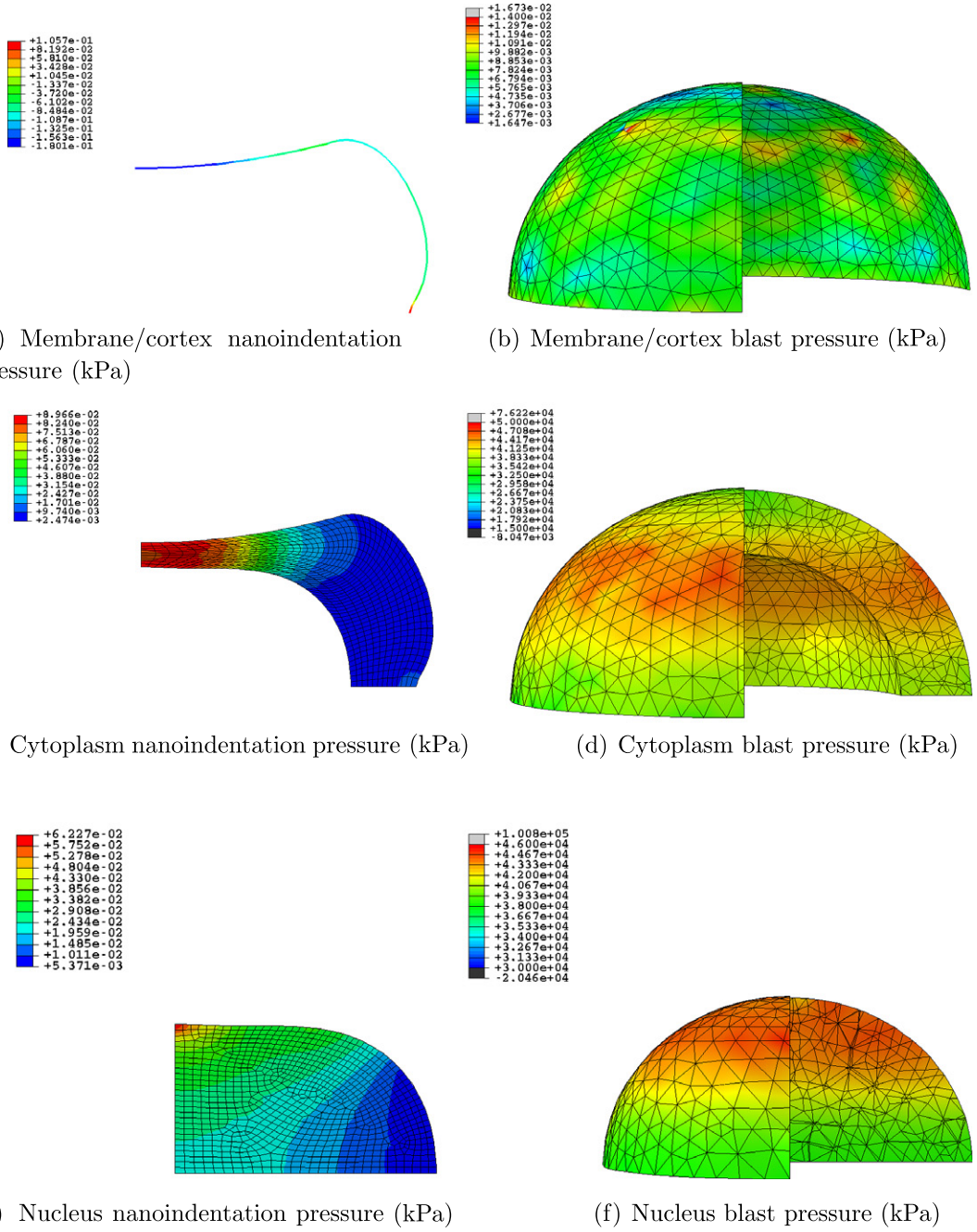

(a) Membrane/cortex nanoindentation pressure (kPa)

(b) Membrane/cortex blast pressure (kPa)

(c) Cytoplasm nanoindentation pressure (kPa)

(d) Cytoplasm blast pressure (kPa)

(e) Nucleus nanoindentation pressure (kPa)

(f) Nucleus blast pressure (kPa)

Fig. 7. Pressure field (kPa) for the nanoindentation and blast simulations at 26.88 s and 65.5 ns, respectively, for the three regions; a quarter of the mesh for the blast simulation has been removed for visualization purposes.

(nanoseconds). However, whereas the shearing forces are concentrated mainly within the nucleus in the nanoindentation case, the maxima can be identified at the interfaces in the blast case.

Finally, it can be seen from Fig. 9 that the temperature is rising by ~0.1 °C.

5. Discussion

The high pressure (~50 MPa) is propagated directly from the water into the cell, and in between the cell parts, mainly because of the lack of a volumetric impedance mismatch (the equation of state parameters are the same). It could thus be relevant to have accurately calibrated parameters for each part of the cell in order to observe the effect of such possible mismatches. However, the volumetric material parameters would still remain relatively similar, and a drastic change in pressure should not be expected. Based on brain tissue studies [48], such high pressure should a priori be sufficient to cause a high degree of brain damage. This conclusion is confirmed by the fact that the rates used here are much higher than those used as tissue damage criteria in other works on impact [26,27] or blast [48,97].

Other works have focused directly on the cell by increasing the pressure up to ~2 MPa (20 atm) over a period of 6 s and sustaining it for 1–10 min [43]. If such work leaves aside the rate effects, it has the benefit of independently identifying the effect of sustained pressure on cell components. Specifically, membrane damage was observed above 10 atm, eventually leading to irreversible damage under sufficient pressure and duration [43]. Additional

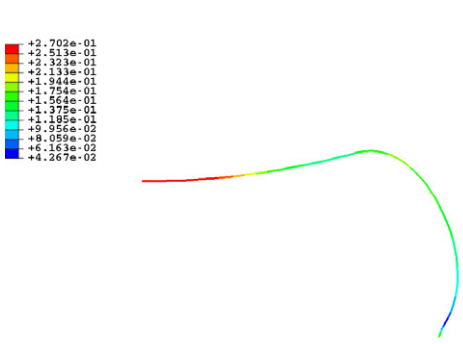

(a) Membrane/cortex nanoindentation von Mises stress (kPa)

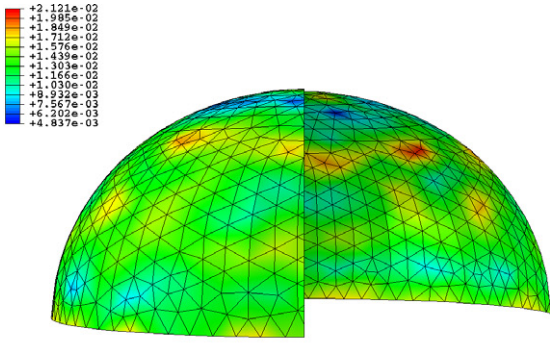

(b) Membrane/cortex blast von Mises stress (kPa)

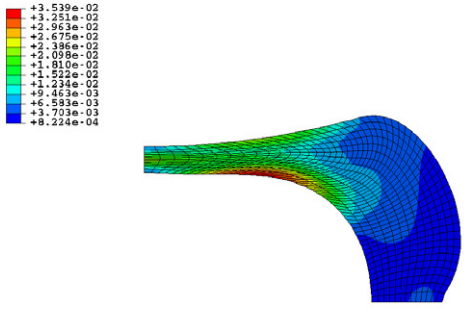

(c) Cytoplasm nanoindentation von Mises stress (kPa)

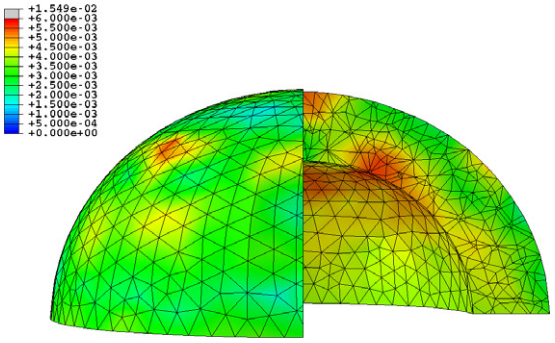

(d) Cytoplasm blast von Mises stress (kPa)

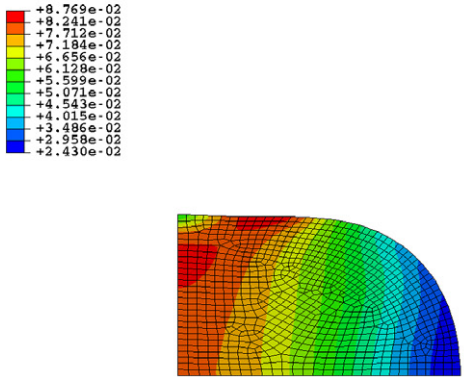

(e) Nucleus nanoindentation von Mises stress (kPa)

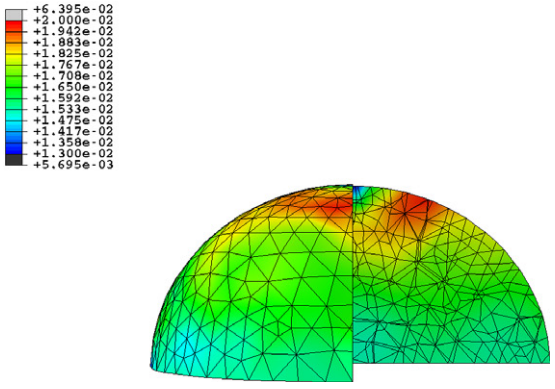

(f) Nucleus blast von Mises stress (kPa)

Fig. 8. Von Mises stress field (kPa) for the nanoindentation and blast simulations at 26.88 s and 65.5 ns, respectively. for the three regions; a quarter of the mesh for the blast simulation has been removed for visualization purposes.

works have similarly focused on the effect of such high hydrostatic pressure on cell functions such as migration [105]. By studying the release of fatty acids and lactate dehydrogenase into the extracellular medium under different pressure levels/durations, Murphy and Horrocks [43] identified damage thresholds for different types of cells. They proposed that, under high pressure, the motion of the membrane's acyl chains is reduced as they condense to accommodate their volume decrease. By so doing, the viscosity is reduced and the "fluid behavior" of the membrane is modified to a stiffer configuration, eventually leading to receptor damage [43]. Along the same lines, recent work by Alford et al. suggests that, under rapid blast-driven stretching, the stimulation of cellular membrane integrins is altered, thus potentially modifying the calcium dynamics and phenotypic behavior in the affected cells [17].

Such experimental findings are corroborated by the von Mises stress fields in Fig. 8. These results show that one of the main features of a blast event is the localized concentration of the von Mises stress at the interfaces within the blast wave plane. The resulting interface shearing effect could have drastic implications on the organization of receptors, transmembranes organelles and associated cytoskeletal components (e.g. in the cortex). The coupling effect of the mechanical loading of the membrane receptors due to pressure and shearing at the interface could thus lead to their alteration. More specifically, the loss of membrane integrity,

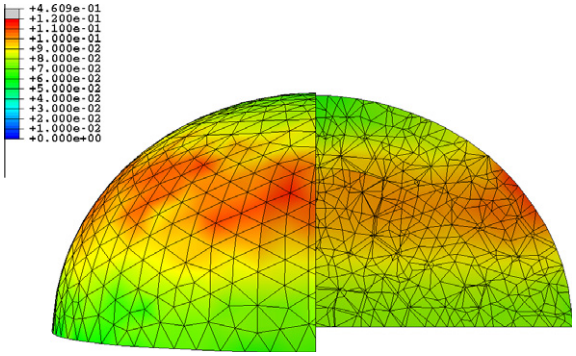

Fig. 9. Temperature increase field (K) for the blast simulation at 65.5 ns for the whole cell; a quarter of the mesh has been removed for visualization purposes.

despite the presence of reversible repair mechanisms below some pressure/duration limits, is a common type of damage in all catastrophic types of cell death. For instance, apoptosis and the detachment of the F-actin cortex from the membrane have been directly related [106], and a direct relation between cell death and loss of membrane integrity has also been observed in necrosis and necroptosis [107–109]. The recent work of Alford et al. on the role of integrin alteration in phenotypic switching confirms that point [17]. Note finally that, to the best of our knowledge, no experimental findings of loss of integrity of the nucleus membrane have been reported. However, the model predicts similar shear stress levels at both the nucleus membrane and the overall cell membrane, and thus potentially similar damage patterns for both the nucleus and cell membranes.

Using shock tube experimental set-ups with different configurations, Reneer et al. have recently highlighted a direct correlation between a longer positive phase duration and a higher level of damage at the same peak pressure [42]. In order to compare this experimentally observed trend to our numerical predictions, the initial shock positive phase duration was extended from 5 ns to 10 and 15 ns. The pressure, von Mises stress, longitudinal (in the shock direction) strain and longitudinal strain rate evolutions for a material point situated along the interface between the cytoplasm and the nucleus at roughly 75% of the total height of the nucleus were measured (see Fig. 10). The results confirm the experimental findings by predicting higher pressure, von Mises stress, strain and strain rate with increasing durations. The von Mises stress level, in particular, has been found to increase proportionally with the duration (doubling and tripling for doubled and tripled durations), thus potentially aggravating the effect of shearing at the interface. The strain rate, however, was found to increase only moderately.

As a consequence, our simulations confirm that laser-induced shock wave experiments on cells lead to interface damage within the cell. The fact that a blast wave seems to concentrate shear forces at these particular regions while potentially debilitating some of its functions through pressure-dependent structural reorganization of the membrane is even more relevant for neurons. Indeed, whereas large strains seem to be sustained by the axon membrane at low rates, high rates of deformation are known to drastically affect the conduction and thus functional properties of axons [110]. This confirms that the model prediction of shear localization at the cortex, potentially exacerbated by a longer positive phase duration, has direct implications on the functional properties of the neuron, and consequently the brain.

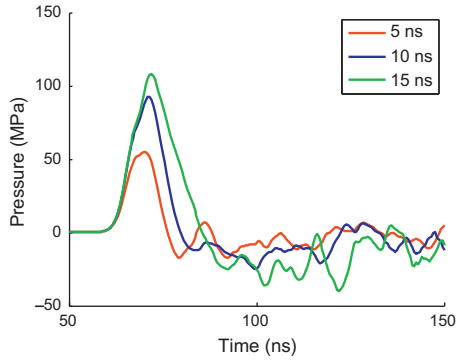

(a) Pressure evolution (MPa)

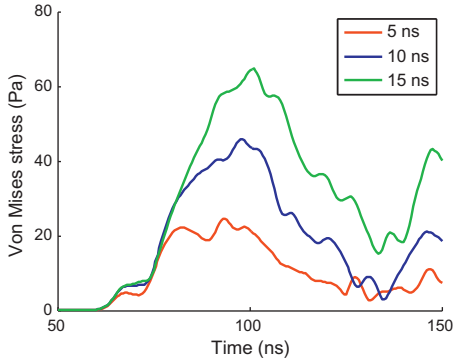

(b) Von Mises stress evolution (Pa)

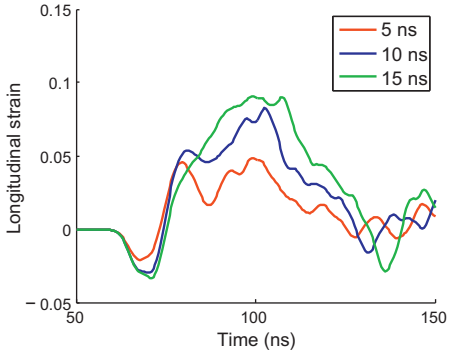

(c) Longitudinal strain evolution

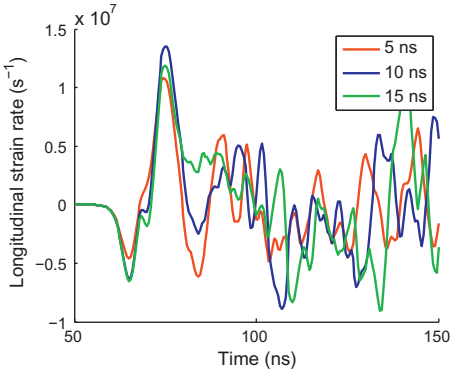

(d) Longitudinal strain-rate evolution (s^{-1})

Fig. 10. Pressure, von Mises stress, longitudinal strain and strain rate evolution at the nucleus–cytoplasm interface, at ~75% of the nucleus height, for three initial positive phase durations: 5, 10 and 15 ns.

Finally, the temperature rise (see Fig. 9) can a priori be judged as too small to damage the cell and/or affect the cell's health. Accordingly, although thermal shock has been shown to have a significant impact on cytoskeletal organization, potentially leading to microtubule malfunctions [111], the experimental temperature change used in that reference is two orders of magnitude higher than here. However, it must be emphasized that the increase of 0.1 °C observable in the cell is achieved in roughly 5 ns, which corresponds to a rate of 20 million °C s^{-1}. It is thus not clear if the temperature rate itself, and not just the level reached, is relevant to the cell's health. Molecular dynamics studies could potentially allow for further investigations in this direction.

6. Conclusion

In this work, a comprehensive continuum model of a neuron was presented. This model involves the consideration of three independent regions: the nucleus, the cytoplasm and the cortex plus membrane. Each region is described by a constitutive model based on visco-hyperelasticity and an equation of state for high rate/pressure loadings. The parameters that were not taken from the literature were calibrated against published experimental multi-rate indentation results. Finally, a blast event within typical in vitro conditions was simulated.

The results show that, whereas the pressure level affects the cell homogeneously, shearing effects are observed mainly at the interfaces. This phenomenon has been shown to be critically important for the integrity and health of cell membranes, confirming what was observed experimentally at the cell function level. Finally, both the pressure and the von Mises stress, and thus the potential damage, have been observed to increase significantly with increased positive phase duration of the shock wave.

In conclusion, the presented model successfully captures some of the intrinsic intracellular phenomena that occur during the rate-dependent neuron deformation and potentially lead to damage. It also predicts that the nucleus membrane is likely to suffer from the same type of damage as has been observed for the cell membrane. Ultimately, the proposed model constitutes a novel numerical tool that is able to predict some of the most complex cell deformation mechanisms occurring during traumatic brain injury.

Acknowledgements

The authors thank Prof. Subra Suresh for his insightful guidance and suggestions. The authors are also grateful to Javier Rodriguez, of Principia, for his immeasurable help with Abaqus. A.J. acknowledges support from the Juan de la Cierva grant from the Spanish Ministry of Science and Innovation, from the Amarout grant from the European Union, from the ESTRUMAT-S2009/MAT-1585 grant (Madrid Regional Government), and from the Cajal Blue Brain Project. M.D. acknowledges support from the National Institutes of Health (NIH) Grant R01HL094270, Infectious Disease Interdisciplinary Research Group of the SMART Center, and the Computational Systems Biology Programme of the Singapore–MIT Alliance (SMA).

Appendix A. Figures with essential colour discrimination

Certain figures in this article, particularly Figs. 2–10, are difficult to interpret in black and white. The full colour images can be found in the on-line version, at http://dx.doi.org/10.1016/j.actbio.2012.04.039.

Appendix B. Supplementary data

Supplementary data associated with this article can be found, in the online version, at http://dx.doi.org/10.1016/j.actbio.2012.04.039.

References

[1] Moore DF, Jaffee MS. Military traumatic brain injury and blast. Neurorehabilitation 2010;26(3):179–81. http://dx.doi.org/10.3233/NRE-2010-0553.
[2] Hicks RR, Fertig SJ, Desrocher RE, Koroshetz WJ, Pancrazio JJ, et al. Neurological effects of blast injury. J Trauma Injury Infect Crit Care 2010;68(5):1257–63. http://dx.doi.org/10.1097/TA.0b013e3181d8956d.
[3] Khan M, Im Y-B, Shunmugavel A, Gilg AG, Dhindsa RK, Singh AK, et al. Administration of S-nitrosoglutathione after traumatic brain injury protects the neurovascular unit and reduces secondary injury in a rat model of controlled cortical impact. J Neuroinflamm 2009;6(32):1–12. http://dx.doi.org/10.1186/1742-2094-6-32.
[4] Norris CM, Scheff SW. Recovery of afferent function and synaptic strength in hippocampal CA1 following traumatic brain injury. J Neurotrauma 2009;26(12):2269–78. http://dx.doi.org/10.1089/neu.2009.1029.
[5] Hunt RF, Scheff SW, Smith BN. Posttraumatic epilepsy after controlled cortical impact injury in mice. Exp Neurol 2009;215:243–52. http://dx.doi.org/10.1016/j.expneurol.2008.10.005.
[6] Shafieian M, Darvish KK, Stone JR. Changes to the viscoelastic properties of brain tissue after traumatic axonal injury. J Biomech 2009;42(13):2136–42. http://dx.doi.org/10.1016/j.jbiomech.2009.05.041.
[7] Kharatishvili I, Sierra A, Immonenb RJ, Gröhn OHJ, Pitkänen A. Quantitative T2 mapping as a potential marker for the initial assessment of the severity of damage after traumatic brain injury in rat. Exp Neurol 2009;217(1):154–64. http://dx.doi.org/10.1016/j.expneurol.2009.01.026.
[8] Chena G, Zhang S, Shi J, Ai J, Qi M, Hang C. Simvastatin reduces secondary brain injury caused by cortical contusion in rats: Possible involvement of TLR4/NF-κB pathway. Exp Neurol 2009;216(2):398–406. http://dx.doi.org/10.1016/j.expneurol.2008.12.019.
[9] Schwetye KE, Cirrito JR, Esparza TJ, Mac Donald CL, Holtzman DM, Brody DL. Traumatic brain injury reduces soluble extracellular amyloid-β in mice: a methodologically novel combined microdialysis-controlled cortical impact study. Neurobiol Dis 2010;40(3):555–64. http://dx.doi.org/10.1016/j.nbd.2010.06.018.
[10] Kabadi SV, Hilton GD, Stoica BA, Zapple DN, Faden AI. Fluid-percussion-induced traumatic brain injury model in rats. Nat Protocol 2010;5(9):1552–63. http://dx.doi.org/10.1038/nprot.2010.112.
[11] Ouyang H, Galle B, Li J, Nauman E, Shi R. Biomechanics of spinal cord injury: a multimodal investigation using ex vivo guinea pig spinal cord white matter. J Neurotrauma 2008;25:19–29. http://dx.doi.org/10.1089/neu.2007.0340.
[12] Connell S, Gao J, Chen J, Shi R. Novel model to investigate blast injury in the central nervous system. J Neurotrauma 2011;28:1229–36. http://dx.doi.org/10.1089/neu.2011.1832.
[13] Geddes DM, Cargill RS, LaPlaca MC. Mechanical stretch to neurons results in a strain rate and magnitude-dependent increase in plasma membrane permeability. J Neurotrauma 2003;20(10):1039–49. http://dx.doi.org/10.1089/089771503770195885.
[14] Geddes-Klein KSDM, Meaney D. Mechanisms and consequences of neuronal stretch injury in vitro differ with the model of trauma. J Neurotrauma 2006;23(2):193–204. http://dx.doi.org/10.1089/neu.2006.23.193.
[15] LaPlaca MC, Prado GR. Neural mechanobiology and neuronal vulnerability to traumatic loading. J Biomech 2010;43(1):71–8. http://dx.doi.org/10.1016/j.jbiomech.2009.09.011.
[16] Ziegler L, Segal-Ruder Y, Coppola G, Reis A, Geschwind D, Fainzilber M, et al. A human neuron injury model for molecular studies of axonal regeneration. Exp Neurol 2010;223(1):119–27. http://dx.doi.org/10.1016/j.expneurol.2009.09.019.
[17] Alford PW, Dabiri BE, Goss JA, Hemphill MA, Brigham MD, Parker KK. Blast-induced phenotypic switching in cerebral vasospasm. PNAS 2011;108(31):12705–10. http://dx.doi.org/10.1073/pnas.1105860108.
[18] Barnes PD, Krasnokutsky MV, Monson KL, Ophoven J. Traumatic spinal cord injury: accidental versus nonaccidental injury. Semin Pediatr Neurol 2008;15(4):178–84. http://dx.doi.org/10.1016/j.spen.2008.10.009.
[19] Hoffman SW, Harrison C. The interaction between psychological health and traumatic brain injury: a neuroscience perspective. Clin Neuropsychol 2009;23:1400–15. http://dx.doi.org/10.1080/13854040903369433.
[20] Yoganandan N, Baisden JL, Maiman DJ, Gennarelli TA, Guan Y, Pintar FA, et al. Severe-to-fatal head injuries in motor vehicle impacts. Accident Anal Prevent 2010;42(4):1370–8. http://dx.doi.org/10.1016/j.aap.2010.02.017.
[21] Goldstein LE, Fisher AM, Tagge CA, Zhang X-L, Velisek L, Sullivan JA, et al. Chronic traumatic encephalopathy in blast-exposed military veterans and a blast neurotrauma mouse model. Sci Transl Med 2012;4(134ra60):1–17. http://dx.doi.org/10.1126/scitranslmed.3003716.
[22] Willinger R, Baumgartner D, Guimberteau T. Dynamic characterization of motorcycle helmets: modelling and coupling with the human head. J Sound Vib 2000;235(4):611–25. http://dx.doi.org/10.1006/jsvi.1999.2931.

[23] Gilchrist MD, O'Donoghue D, Horgan T. A two-dimensional analysis of the biomechanics of frontal and occipital head impact injuries. Int J Crashworthiness 2000;6(2):253–62. http://dx.doi.org/10.1533/cras.2001.0176.

[24] Willinger R, Baumgartner D, Chinn B, Schuller E. New dummy head prototype: development, validation and injury criteria. International Journal of Crashworthiness 2000;6(3):281–94. http://dx.doi.org/10.1533/cras.2001.0178.

[25] Guillaume AI, Osmont D, Gaffié D, Sarron J-C, Quandieu P. Physiological implications of mechanical effects of +Gz accelerations on brain structures. Aviation Space Environ Med 2002;73(3):171–7.

[26] Willinger R, Baumgartner D. Human head tolerance limits to specific injury mechanisms. Int J Crashworthiness 2003;8(6):605–17. http://dx.doi.org/10.1533/ijcr.2003.0264.

[27] Willinger R, Baumgartner D. Numerical and physical modelling of the human head under impact – towards new injury criteria. Int J Vehicle Des 2003;32(1–2):94–115. http://dx.doi.org/10.1504/IJVD.2003.003239.

[28] Horgan TJ, Gilchrist MD. The creation of three-dimensional finite element models for simulating head impact biomechanics. Int J Crashworthiness 2003;8(4):353–66. http://dx.doi.org/10.1533/ijcr.2003.0243.

[29] Zhang L, Yang KH, King AI. A proposed injury threshold for mild traumatic brain injury. Trans ASME 2004;126:226–36.

[30] Horgan TJ, Gilchrist MD. Influence of FE model variability in predicting brain motion and intracranial pressure changes in head impact simulations. Int J Crashworthiness 2004;9(4):401–18. http://dx.doi.org/10.1533/ijcr.2004.0299.

[31] Raul J-S, Baumgartner D, Willinger R, Ludes B. Finite element modelling of human head injuries caused by a fall. Int J Legal Med 2006;120(4):212–8. http://dx.doi.org/10.1007/s00414-005-0018-1.

[32] El Sayed T, Mota A, Fraternali F, Ortiz M. Biomechanics of traumatic brain injury. Comput Method Appl Mech Eng 2008;197(51–52):4692–701. http://dx.doi.org/10.1016/j.cma.2008.06.006.

[33] Deck C, Willinger R. Improved head injury criteria based on head FE model. Int J Crashworthiness 2008;13(6):667–79. http://dx.doi.org/10.1080/13588260802411523.

[34] Abolfathi N, Karami G, Ziejewski M. Biomechanical cell modeling under impact loading. Int J Model Simul 2008;28(4):470–6. http://dx.doi.org/10.2316/Journal.205.2008.4.205-4877.

[35] Motherway J, Doorly MC, Curtis M, Gilchrist MD. Head impact biomechanics simulations: a forensic tool for reconstructing head injury? Legal Med 2009;11(1):S220–2. http://dx.doi.org/10.1016/j.legalmed.2009.01.072.

[36] Christou G, Young LR, Goel R, Vechart A, Jérusalem A. Soda-lime glass based material attenuates shock in a helmet liner: a fluid–solid interaction continuum model simulation. Int J Impact Eng. 2010;47:48–59. http://dx.doi.org/10.1016/j.ijimpeng.2012.03.003.

[37] Mayorga MA. The pathology of primary blast overpressure injury. Toxicology 1997;121:17–28. http://dx.doi.org/10.1016/S0300-483(97)03652-4.

[38] Warden DL, French LM, Shupenko L, Fargus J, Riedy G, Erickson ME, et al. Case report of a soldier with primary blast brain injury. Neuroimage 2009;47(2):T152–3. http://dx.doi.org/10.1016/j.neuroimage.2009.01.060.

[39] Cernak I, Noble-Haeusslein LJ. Traumatic brain injury: an overview of pathobiology with emphasis on military populations. J Cereb Blood Flow Metab 2010;30:255–66. http://dx.doi.org/10.1038/jcbfm.2009.203.

[40] Leung LY, VandeVord PJ, Dal Cengio AL, Bir C, Yang KH, King AI. Blast related neurotrauma: a review of cellular injury. Mol Cell Biomech 2008;5(3):155–68.

[41] Chavko M, Koller WA, Prusaczyk WK, McCarron RM. Measurement of blast wave by a miniature fiber optic pressure transducer in the rat brain. J Neurosci Method 2007;159:277–81. http://dx.doi.org/10.1016/j.jneumeth.2006.07.018.

[42] Reneer DV, Hisel RD, Hoffman JM, Kryscio RJ, Lusk BT, Geddes JW. A multi-mode shock tube for investigation of blast-induced traumatic brain injury. J Neurotrauma 2011;28:95–104. http://dx.doi.org/10.1089/neu.2010.1513.

[43] Murphy EJ, Horrocks LA. A model for compression trauma: pressure-induced injury in cell cultures. J Neurotrauma 1993;10(4):431–43. http://dx.doi.org/10.1089/neu.1993.10.431.

[44] Chen YC, Smith DH, Meaney DF. In-vitro approaches for studying blast-induced traumatic brain injury. J Neurotrauma 2009;26:861–76. http://dx.doi.org/10.1089/neu.2008.0645.

[45] Prevost TP, Jin G, de Moya MA, Alam HB, Suresh S, Socrate S. Dynamic mechanical response of brain tissue in indentation in vivo, in situ and in vitro. Acta Biomater 2011;7(12):4090–101. http://dx.doi.org/10.1016/j.actbio.2011.06.032.

[46] Huang B, Babcock H, Zhuang X. Breaking the diffraction barrier: super-resolution imaging of cells. Cell 2010;25:1047–58. http://dx.doi.org/10.1016/j.cell.2010.12.002.

[47] Moss WC, King MJ, Blackman EG. Skull flexure from blast waves: a mechanism for brain injury with implications for helmet design. Phys Rev Lett 2009;103(108702):1–4. http://dx.doi.org/10.1103/PhysRevLett.103.108702.

[48] Moore DF, Jérusalem A, Nyein M, Noels L, Jaffee MS, Radovitzky RA. Computational biology – modeling of primary blast effects on the central nervous system. Neuroimage 2009;47(2):T10–20. http://dx.doi.org/10.1016/j.neuroimage.2009.02.019.

[49] Karen Lee KY, Nyein MK, Moore DF, Joannopoulos JD, Socrate S, Imholt T, et al. Blast-induced electromagnetic fields in the brain from bone piezoelectricity. Neuroimage 2010;54(S1):S30–6. http://dx.doi.org/10.1016/j.neuroimage.2010.05.042.

[50] Nyein MK, Jason AM, Yu L, Pita CM, Joannopoulos JD, Moore DF, et al. In silico investigation of intracranial blast mitigation with relevance to military traumatic brain injury. PNAS 2010;107(48):20703–8. http://dx.doi.org/10.1073/pnas.1014786107.

[51] Kamm RD, McVittie AK, Bathe M. On the role of continuum models in mechanobiology. Mech Biol – ASME 2000;242:1–11.

[52] Guilak F, Tedrow JR, Burgkart R. Viscoelastic properties of the cell nucleus. Biochem Biophys Res Commun 2000;269:781–6. http://dx.doi.org/10.1006/bbrc.2000.2360.

[53] Mijailovich SM, Kojic M, Zivkovic M, Fabry B, Fredberg JJ. A finite element model of cell deformation during magnetic bead twisting. J Appl Physiol 2002;93:1429–36. http://dx.doi.org/10.1152/japplphysiol.00255.2002.

[54] Caille N, Thoumine O, Tardy Y, Meister J-J. Contribution of the nucleus to the mechanical properties of endothelial cells. J Biomech 2002;35(2):177–87. http://dx.doi.org/10.1016/S0021-929(01)00201-9.

[55] Dao M, Lim CT, Suresh S. Mechanics of the human red blood cell deformed by optical tweezers. J Mech Phys Solids 2003;51:2259–80. http://dx.doi.org/10.1016/j.jmps.2003.09.019.

[56] Karcher H, Lammerding J, Huang H, Lee RT, Kamm RD, Kaazempur-Mofrad MR. A three-dimensional viscoelastic model for cell deformation with experimental verification. Biophys J 2003;85:3336–49. http://dx.doi.org/10.1016/S0006-349(03)74753-5.

[57] McGarry JG, Prendergast PJ. A three-dimensional finite element model of an adherent eukaryotic cell. Eur Cell Mater 2004;7:27–33.

[58] McNally HA, Ben Borgens R. Three-dimensional imaging of living and dying neurons with atomic force microscopy. J Neurocytol 2004;33:251–8. http://dx.doi.org/10.1023/B:NEUR.0000030700.48612.0b.

[59] Jean RP, Chen CS, Spector AA. Finite-element analysis of the adhesion-cytoskeleton-nucleus mechanotransduction pathway during endothelial cell rounding: axisymmetric model. J Biomech Eng 2005;127:594–600. http://dx.doi.org/10.1115/1.1933997.

[60] Peeters AG, Oomens CWJ, Bouten CVC, Bader DL, Baaijens FPT. Viscoelastic properties of single attached cells under compression. J Biomech Eng 2005;127:237–43. http://dx.doi.org/10.1115/1.1865198.

[61] Lim CT, Zhou EH, Quek ST. Mechanical models for living cells—a review. J Biomech 2006:195–216. http://dx.doi.org/10.1016/j.jbiomech.2004.12.008.

[62] Mofrad MRK, Kamm RD. Cytoskeletal mechanics, models and measurements. Cambridge University Press; 2006.

[63] Vaziri A, Lee H, Mofrad MRK. Deformation of the cell nucleus under indentation: mechanics and mechanisms. J Mater Res 2006;21(8):2126–35. http://dx.doi.org/10.1557/JMR.2006.0262.

[64] Lu Y-B, Franze K, Seifert G, Steinhauser C, Kirchhoff F, Wolburg H, et al. Viscoelastic properties of individual glial cells and neurons in the CNS. PNAS 2006;103(47):17759–64. http://dx.doi.org/10.1073/pnas.0606150103.

[65] Flaherty B, McGarry JP, McHugh PE. Mathematical models of cell motility. Cell Biochem Biophys 2007;49(1):25–8. http://dx.doi.org/10.1007/s12013-007-0045-2.

[66] Suresh S. Biomechanics and biophysics of cancer cells. Acta Biomater 2007;3:413–38. http://dx.doi.org/10.1016/j.actbio.2007.04.002.

[67] Gladilin E, Micoulet A, Hosseini B, Rohr K, Spatz J, Eils R. 3D finite element analysis of uniaxial cell stretching: from image to insight. Phys Biol 2007;4(2):104–13. http://dx.doi.org/10.1088/1478-3975/4/2/004.

[68] Zhang CY, Zhang YW. Effects of membrane pre-stress and intrinsic viscoelasticity on nanoindentation of cells using AFM. Philos Mag 2007;87:3415–35. http://dx.doi.org/10.1080/14786430701288094.

[69] Moreo P, García-Aznar JM, Doblaré M. Modeling mechanosensing and its effect on the migration and proliferation of adherent cells. Acta Biomater 2008;4:613–21. http://dx.doi.org/10.1016/j.actbio.2007.10.014.

[70] Mandadapu KK, Govindjee S, Mofrad MRK. On the cytoskeleton and soft glassy rheology. J Biomech 2008;41:1467–78. http://dx.doi.org/10.1016/j.jbiomech.2008.02.014.

[71] Ingber DE. Tensegrity-based mechanosensing from macro to micro. Prog Biophys Mol Biol 2008;97:163–79. http://dx.doi.org/10.1016/j.pbiomolbio.2008.02.005.

[72] Zhang CY, Zhang YW. Computational analysis of adhesion force in the indentation of cells using atomic force microscopy. Phys Rev E 2008;77:021912. http://dx.doi.org/10.1103/PhysRevE.77.021912.

[73] Ofek G, Natoli RM, Athanasiou KA. In situ mechanical properties of the chondrocyte cytoplasm and nucleus. J Biomech 2009;42:873–7. http://dx.doi.org/10.1016/j.jbiomech.2009.01.024.

[74] McGarry JP. Characterization of cell mechanical properties by computational modeling of parallel plate compression. Ann Biomed Eng 2009;37:2317–25. http://dx.doi.org/10.1007/s10439-009-9772-4.

[75] Allena R, Mouronval A-S, Aubry D. Simulation of multiple morphogenetic movements in the drosophila embryo by a single 3D finite element model. J Mech Behav Biomed Mater 2010;3(4):313–23. http://dx.doi.org/10.1016/j.jmbbm.2010.01.001.

[76] Young J, Mitran S. A numerical model of cellular blebbing: a volume-conserving, fluid–structure interaction model of the entire cell. J Biomech 2010;43(2):210–20. http://dx.doi.org/10.1016/j.jbiomech.2009.09.025.

[77] Miller P, Hu L, Wang J. Finite element simulation of cell–substrate decohesion by laser-induced stress waves. J Mech Behav Biomed Mater 2010;3(3):268–77. http://dx.doi.org/10.1016/j.jmbbm.2009.11.001.

[78] Bernick KB, Prevost TP, Suresh S, Socrate S. Biomechanics of single cortical neurons. Acta Biomater 2011;7(3):1210–9. http://dx.doi.org/10.1016/j.actbio.2010.10.018.
[79] Dintwa E, Jancsók P, Mebatsion HK, Verlinden B, Verboven P, Wang CX, et al. A finite element model for mechanical deformation of single tomato suspension cells. Journal of Food Engineering 2010;103(3):265–72. http://dx.doi.org/10.1016/j.jfoodeng.2010.10.023.
[80] Yan KC, Nair K, Sun W. Three dimensional multi-scale modelling and analysis of cell damage in cell-encapsulated alginate constructs. J Biomech 2010;43(6):1031–8. http://dx.doi.org/10.1016/j.jbiomech.2009.12.018.
[81] Slomka N, Gefen A. Confocal microscopy-based three-dimensional cell-specific modeling for large deformation analyses in cellular mechanics. J Biomech 2010;43:1806–16. http://dx.doi.org/10.1016/j.jbiomech.2010.02.011.
[82] Dao M, Li J, Suresh S. Molecularly based analysis of deformation of spectrin network and human erythrocyte. Mater Sci Eng C 2006;26:1232–44. http://dx.doi.org/10.1016/j.mSection 2005.08.020.
[83] Li J, Lykotrafitis G, Dao M, Suresh S. Cytoskeletal dynamics of human erythrocyte. PNAS 2007;104:4937–42. http://dx.doi.org/10.1073/pnas.0700257104.
[84] Quinn DJ, Pivkin I, Wong SY, Chiam K-H, Dao M, Karniadakis GE, et al. Combined simulation and experimental study of large deformation of red blood cells in microfluidic systems. Ann Biomed Eng 2011;39:1041–50. http://dx.doi.org/10.1007/s10439-010-0232-y.
[85] Diez-Silva M, Dao M, Han J, Lim C-T, Suresh S. Shape and biomechanical characteristics of human red blood cells in health and disease. MRS Bull 2010;35:382–8. http://dx.doi.org/10.1557/mrs2010.571.
[86] Kaplus M, Kuriyan J. Molecular dynamics and protein function. PNAS 2005;102(19):6679–85. http://dx.doi.org/10.1073/pnas.0408930102.
[87] Ayton GS, Voth GA. Multiscale simulation of protein mediated membrane remodeling. Semin Cell Dev Biol 2010;21(4):357–62. http://dx.doi.org/10.1016/j.semcdb.2009.11.011.
[88] Deriu MA, Bidone TC, Mastrangelo F, Di Benedetto G, Soncini M, Montevecchi FM, et al. Biomechanics of actin filaments: a computational multi-level study. J Biomech, in press. http://dx.doi.org/10.1016/j.jbiomech.2010.11.014.
[89] Hu L, Zhang X, Miller P, Ozkan M, Ozkan C, Wang J. Cell adhesion measurement by laser-induced stress waves. J Appl Phys 2006;100(084701):1–5. http://dx.doi.org/10.1063/1.2356107.
[90] Holzapfel GA. Nonlinear solid mechanics. John Wiley & Sons; 2000.
[91] Taylor RL, Pister KS, Goudreau GL. Thermomechanical analysis of viscoelastic solids. Int J Numer Method Eng 1970;2(1):45–59. http://dx.doi.org/10.1002/nme.1620020106.
[92] Kaliske M, Rothert H. Formulation and implementation of three-dimensional viscoelasticity at small and finite strains. Comput Mech 1997;19(3):228–39. http://dx.doi.org/10.1007/s004660050171.
[93] Meyers Marc A. Dynamic behavior of materials. Wiley–Interscience; 1994.
[94] Drumheller DS. Introduction to wave propagation in nonlinear fluids and solids. Cambridge University Press; 1998.
[95] Conde C, Cáceres A. Microtubule assembly, organization and dynamics in axons and dendrites. Nat Rev Neurosci 2009;10:319–32. http://dx.doi.org/10.1038/nrn2631.
[96] Simulia, Abaqus 6.10; 2010.
[97] Matthew David Alley. Explosive blast loading experiments for TBI scenarios: characterization and mitigation. Master's thesis, Purdue University; 2009.
[98] Sondén A, Svensson B, Roman N, Ostmark H, Brismar B, Palmblad J, et al. Laser-induced shock wave endothelial cell injury. Lasers Surg Med 2000;26:364–75. http://dx.doi.org/10.1002/(SICI)1096-9101(2000)26:4.
[99] Guilak F. Compression-induced changes in the shape and volume of the chondrocyte nucleus. J Biomech 1995;28:1529–41. http://dx.doi.org/10.1016/0021-929(95)00100-X.
[100] Nagayama K, Mori Y, Shimada K. Shock Hugoniot compression curve for water up to 1 GPa by using a compressed gas gun. J Appl Phys 2002;91(1):476–82. http://dx.doi.org/10.1063/1.1421630.
[101] Boehler R, Kennedy G. Pressure dependence of the thermodynamical Grüneisen parameters of fluids. J Appl Phys 1977;48(10):4183–6.
[102] Barron THK, White GK. Heat capacity and thermal expansion at low temperatures. Kluwer Academic/Plenu; 1999.
[103] Bett KE, Cappi JB. Effect of pressure on the viscosity of water. Nature 1965;207:620–1. http://dx.doi.org/10.1038/207620a0.
[104] Nagayama K, Mori Y, Motegi Y, Nakahara K. Shock Hugoniot for biological materials. Shock Waves 2006;15:267–75. http://dx.doi.org/10.1007/s00193-006-0030-5.
[105] Salvador-Silva M, Aoi S, Parker A, Yang P, Pecen P, Hernandez MR. Responses and signaling pathways in human optic nerve head astrocytes exposed to hydrostatic pressure in vitro. Glia 2003;45(4):364–77. http://dx.doi.org/10.1002/glia.10342.
[106] Stricker J, Falzone T, Gardel ML. Mechanics of the F-actin cytoskeleton. J Biomech 2010;43(1):9–14. http://dx.doi.org/10.1016/j.jbiomech.2009.09.003.
[107] McCall K. Genetic control of necrosis—another type of programmed cell death. Curr Opin Cell Biol 2010;22(6):882–8. http://dx.doi.org/10.1016/j.ceb.2010.09.002.
[108] Challa S, Ka-Ming Chan F. Going up in flames: necrotic cell injury and inflammatory diseases. Cell Mol Life Sci 2000;67(19):3241–53. http://dx.doi.org/10.1007/s00018-010-0413-8.
[109] Christofferson DE, Yuan J. Necroptosis as an alternative form of programmed cell death. Curr Opin Cell Biol 2010;22(2):263–8. http://dx.doi.org/10.1016/j.ceb.2009.12.003.
[110] Shi R, Whitebone J. Conduction deficits and membrane disruption of spinal cord axons as a function of magnitude and rate of strain. J Neurophysiol 2006;95(6):3384–90. http://dx.doi.org/10.1152/jn.00350.2005.
[111] Suzuki H, Kumai T, Matsuzaki M. Effect of temperature decline on the cytoskeletal organization of the porcine oocyte. J Mammal Ova Res 2007;24:107–13. http://dx.doi.org/10.1274/jmor.24.107.